Mathematical Biosciences and Engineering

MBE, 16(6): 7494–7509.
DOI: 10.3934/mbe.2019376
Received: 08 March 2019
Accepted: 31 July 2019
Published: 19 August 2019

http://www.aimspress.com/journal/MBE

Research article

Combined effect of M/A constituent and grain boundary on the impact toughness of CGHAZ and ICCGHAZ of E550 grade offshore engineering steel

Xuelin Wang[1,2], Zhiquan Wang[1], Zhenjia Xie[1], Xiaoping Ma[3], Sundaresa Subramanian[4], Chengjia Shang[1,5,*], Xiucheng Li[1] and Jingliang Wang[1,*]

[1] Collaborative Innovation Center of Steel Technology, University of Science and Technology Beijing, Beijing 100083, China
[2] Management Committee of High-tech Industrial Development Zone of Tongliang, Chongqing 402560, China
[3] Algoma Steel Inc., Sault Ste. Marie P6A 7B4, Canada
[4] Department of Materials Science and Engineering, McMaster University, Hamilton L8S 4L7, Canada
[5] State Key Laboratory of Metal Materials for Marine Equipment and Applications, Anshan, Liaoning 114021, China

* **Correspondence:** Email: cjshang@ustb.edu.cn, jlwang@ustb.edu.cn.

Abstract: The present paper investigated the relationship between low temperature impact toughness and microstructure of bainite in coarse-grained heat affected zone (CGHAZ) and intercritically rehazed CGHAZ (ICCGHAZ) of an offshore engineering steel from both the microstructure morphological and crystallographic aspects. In this work, six groups of samples simulated CGHAZ and ICCGHAZ were designated at three different cooling rates. The Charpy test results showed that the toughness in CGHAZ decreases dramatically with decrease of cooling rate, which was attributed to the microstructural evolution from lath bainite to granular bainite, accompanying with the size increase of Bain zone and the change of M/A morphology from film to block. The increase in hardenability by cooling rate promotes more crystallographic variants from different Bain groups. Meanwhile, the combination with controlled inter-spacing of block boundaries by self-accommodation below the critical Griffith crack length, micro-crack can be arrested by these high angle grain boundaries thereby suppressed brittle fracture initiation and increased fracture properties. However, the variation in toughness of ICCGHAZ is not a concern, since obtaining

excellent toughness is scarcely accessible even if the matrix microstructure is analogous to CGHAZ. It was due to the formation of coarse M/A constituents (~2 μm) necklacing at the prior austenite grain boundary. The visualized crystallography suggested that the impact toughness was partially correlated to the configuration manner and the size of Bain zones as well via promoting highly misoriented angle (>45 °) boundaries, which in turn effectively deflected or arrested the brittle crack propagation.

Keywords: M/A constituent; crystallography; Bain zone; crack propagation; impact toughness

1. Introduction

Offshore engineering steels with high strength and good toughness have been widely used for construction of the marine structures. Meanwhile, the construction of steel structure has more stringent requirements for welding performance of the base material [1,2]. Since most of the offshore engineering steels are always processed into medium or heavy plates according to the requirements of actual construction, dual-pass and multi-pass welding are unavoidable. However, what comes simultaneously with these welding processes is the formation of heat affected zone (HAZ) adjacent to fusion line, which is often concluded as the most critical region with regard to potential failures, especially coarse grained HAZ (CGHAZ) and intercritically reheated CGHAZ (ICCGHAZ) which always exhibit the worst impact toughness [3,4].

Previous studies [5–9] issued that the most important concern in HAZ is impact toughness, and the critical factors that affect impact energy are M/A (martensite/austenite) constituents and high angle grain boundaries. The size, morphology and volume fraction of M/A constituents, as well as the density and inter-spacing of high angle grain boundaries are several key points to determine the impact energy. For CGHAZ, the formation of M/A constituents and high angle grain boundaries is primarily governed by cooling process, which can be controlled by regulating welding parameters, such as heat input. This has been studied systematically by You [9] and the others [10,11] and concluded that altering the heat input is by far the best way to obtain the optimum microstructure with fine M/A particles and high density of high angle grain boundaries, and good impact toughness. However, for ICCGHAZ, the frequently occurred necklace-type M/A constituents along prior austenite grain boundary has made it scarcely possible to regulate the toughness since they are particularly difficult to be controlled since they are formed in the second thermal cycle with peak temperature locating between Ac1 and Ac3 [3,12]. Moreover, these necklace-type M/A constituents with large size can enrich high carbon and increase cracking sensitivity, and thus change the fracture mechanism from nucleation-controlled to propagation-controlled [13–15], which will promote the propagation of cleavage fracture and thus dramatically reduce the impact toughness. Although, the singular role of M/A and high angle grain boundries on the impact toughness has been certified thoroughly, the combined effect of these two points are not elaborated clearly. Additionally, further investigation on whether precursor microstructure formed in CGHAZ has any positive effect on subsequent microstructure including necklace-type M/A constituents and impact toughness in ICCGHAZ is essential and unignorable.

Therefore, in the present study, the correlation between microstructure and impact toughness in CGHAZ and ICCGHAZ will be studied from both microstrucuctural morphology (M/A) and

crystallography (grain boundary). Moreover, the combined effect of M/A and grain boundary on impact toughness, and the heredity effect of precursor microstructure on subsequent microstructure and impact toughness will also be discussed.

2. Experimental

An E550 grade (yield strength: 550 MPa) offshore engineering steel with chemical composition (wt%) of Fe-0.06C-0.26Si-1.38Mn-0.65Ni-0.044Nb-0.4Cr-0.22Mo-0.35Cu-0.017Ti was employed in the present study. To obtain the microstructure and impact toughness of CGHAZ and ICCGHAZ, single and dual pass thermal simulation were carried out using Gleeble-3500. The simulated thermal cycles are presented in Figure 1. Three cooling rates through the temperature range from 800 to 500 °C corresponding to $\Delta t_{8/5}$ time of 8 (fast cooling), 20 (medium cooling) and 50 (slow cooling) s were designed to obtain different bainitic structures in CGHAZ. For ICCGHAZ, the peak temperature of second pass was fixed at a middle temperature (780 ℃) between Ac1 and Ac3. After thermal simulation, standard impact specimens with the size of 10 mm × 10 mm × 55 mm were prepared to evaluate Charpy V-Notch (CVN) impact toughness at –40 ℃.

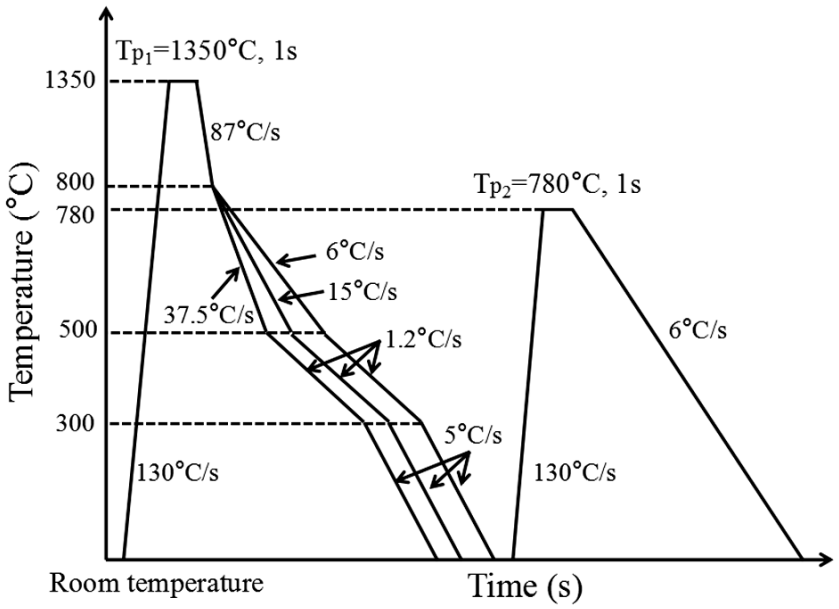

Figure 1. Schematic diagram showing the thermal simulation of CGHAZ and ICCGHAZ.

The microstructure of simulated samples etched with 4% nital was observed first by optical microscopy (OM). Fracture surfaces of the samples after Charpy impact tests and M/A morphology were characterized by scanning electron microscopy (SEM). Electron back-scattered diffraction (EBSD) in the SEM operated at 20 kV was used to study the changes in crystallographic features of bainite induced by cooling rate. Meanwhile, the correlation between crystallographic structure and crack propagation behavior was analyzed by using EBSD. Channel 5 software from Oxford-HKL and ARPGE software [16] were employed for post-processing original EBSD data.

3. Results and discussion

3.1. Charpy impact toughness and fractographs

Figure 2 presents the results of Charpy impact toughness performed at –40 ℃ of the simulated CGHAZ and ICCGHAZ. It can be seen that the average impact energy of CGHAZ declines dramatically from 170 to 27 J with decrease of cooling rate from 37.5 to 6 ℃/s (increase of cooling time $\Delta t_{8/5}$ from 8 to 50 s). Although similar tendency can be found in ICCGHAZ, the decrement is insignificant and only 21 J. Compared with CGHAZ and ICCGHAZ, it can be seen that excellent toughness (170 J) can be obtained in CGHAZ with high cooling rate, but for ICCGHAZ all Charpy values are lower than 45 J. That means the second thermal cycle with peak temperaute between Ac1 and Ac3 will deteriorate the toughness of prior CGHAZ. This result agreed with the previous stduy on impact toughness of HAZ in X100 pipeline steel [4], which suggested that the most vulnerable link usually occurs in ICCGHAZ and subsequently dominates the fracture behavior of the entire weldment.

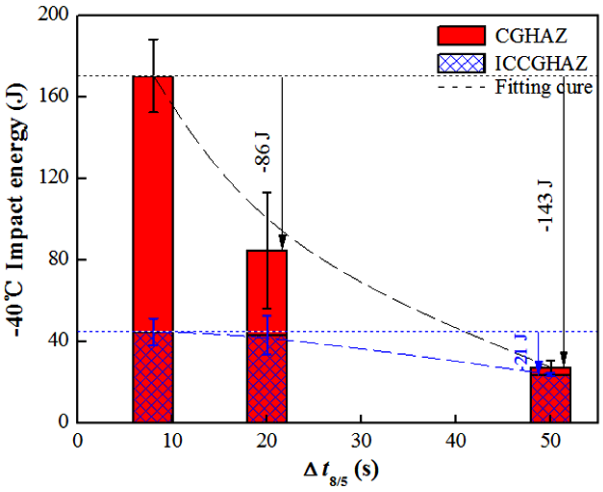

Figure 2. Charpy impact toughness of simulated samples.

Figures 3 and 4 show SEM images of the typical fracture surfaces of all simulated samples. The fracture surfaces shown in CGHAZ (Figure 3) consist of ductile and brittle manners, i.e. dimple and cleavage patterns. There is no visuable difference in morphology of dimple, but the area of ductile fracture region decreases observably with reduction of cooling rates. Moreover, the size of cleavage facets increases, especially as the cooling rate dropped to 6 ℃/s. These varieties in fracture surfaces are very consistent with the decrease in impact toughness. For ICCGHAZ (Figure 4), the fracture surfaces of all the three samples are dominant by cleavage patterns though small size of ductile region is formed as well in high and medium cooling rates, declaring poor toughness. Moreover, the tendencies changing in size of ductile region and cleavage facet are similar to CGHAZ, suggesting the effect of precursor microstructure on impact toughness of ICCGHAZ. Additionally, the reason of why the impact energies of ICCGHAZ with high and medium cooling rates are superior than CGHAZ with low cooling rate is attributed to the formation of larger size of ductile region and finer size of cleavage facet, which will be discussed in the viewpoint of microstructural evolution.

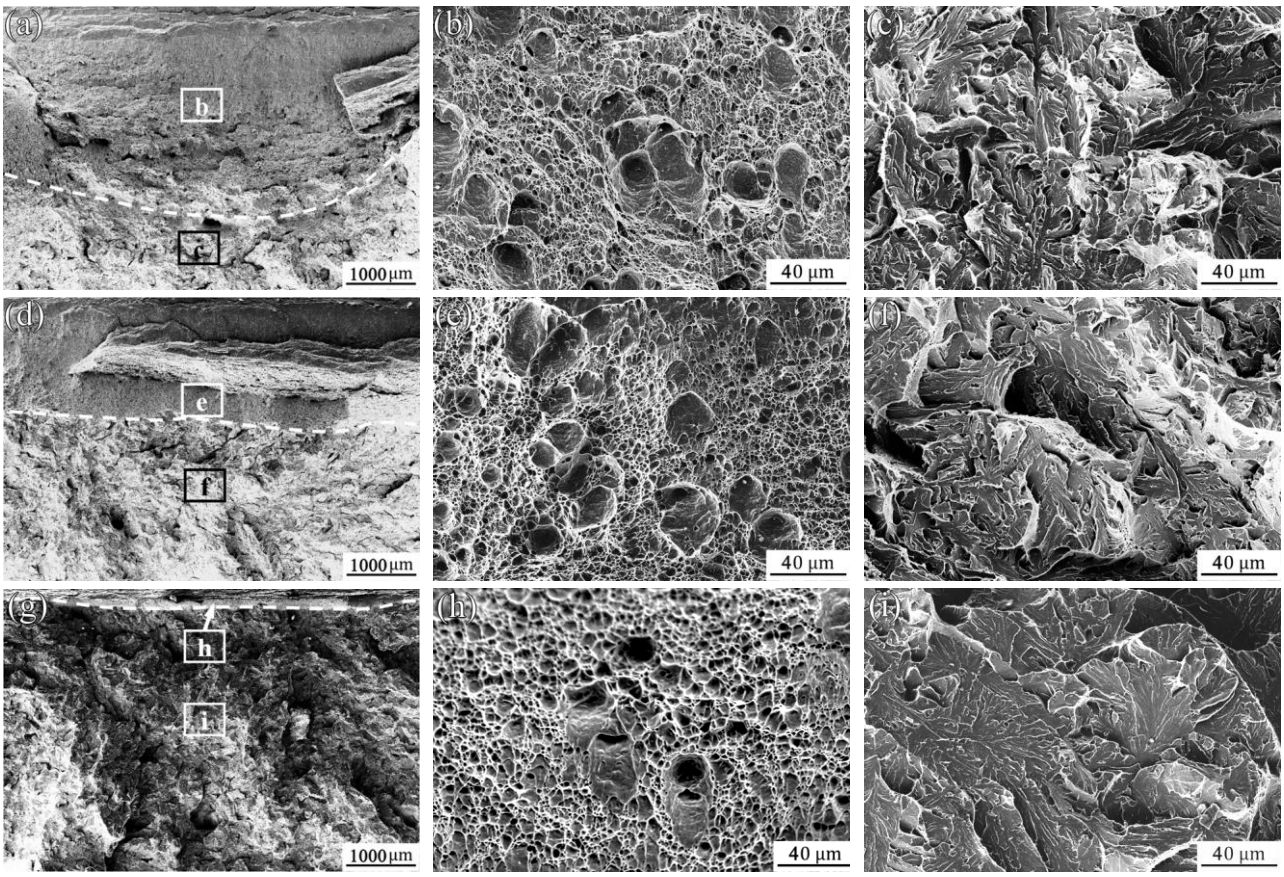

Figure 3. SEM micrographs showing the fracture surface after Charpy impact tests for the simulated samples of CGHAZ: (a–c) $\Delta t_{8/5}$ = 8 s, (d–f) $\Delta t_{8/5}$ = 20 s and (g–i) $\Delta t_{8/5}$ = 50 s.

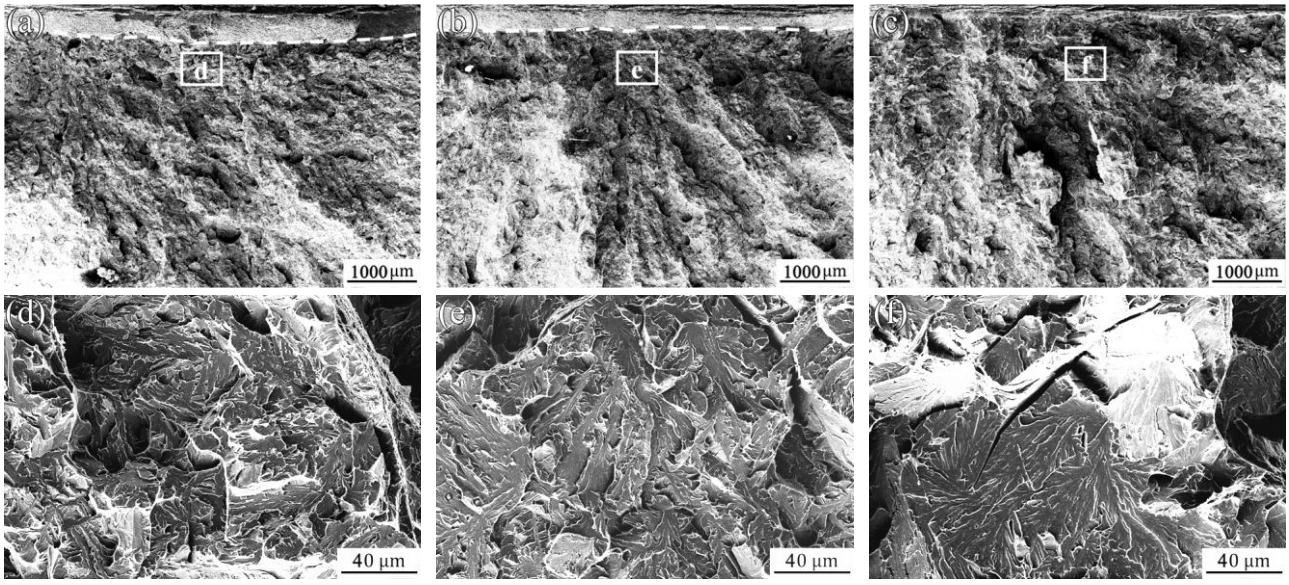

Figure 4. SEM micrographs showing the fracture surface after Charpy impact tests for the simulated samples of ICCGHAZ: (a,d) $\Delta t_{8/5}$ = 8 s, (b,e) $\Delta t_{8/5}$ = 20 s and (c,f) $\Delta t_{8/5}$ = 50 s.

3.2. Microstructural analysis

3.2.1. Optical microstructure

Shown respectively in Figure 5 are the typical microstructures of simulated CGHAZ and ICCGHAZ, which display the characteristic of bainitic structures, i.e. lath bainite (LB) and granular bainite (GB). It can be seen that the microstructures of CGHAZ change from LB to a mixture of LB and GB, and then to full GB with decreasing in cooling rates. Similar results can be obtained in ICCGHAZ, while both of the lath and M/A particles formed in the matrix get coarser. Moreover, the most prominent is large necklace-type M/A constituents formed along prior austenite grain boundaries (PAGB). The above two differences between CGHAZ and ICCGHAZ in coarsen of matrix microstructure and formation of necaklace-type M/A constituents are due to the second thermal cycle process. Since the second peak temperature was located in two phase region (Ac1–Ac3), only part of the matrix microstructure obtained in CGHAZ was reverted to austenite [3]. The reversed austenite islands preferentially nucleated at PAGB and became enriched in carbon, and subsequently transformed to M/A particles during cooling, forming a "necklace" around the prior austenite grain. Moreover, the combined effect of coalescence, heredity and separation of the precursor microstructure that promoted the final microstructural morphology of ICCGHAZ was similar to CGHAZ, except for the size coarsening.

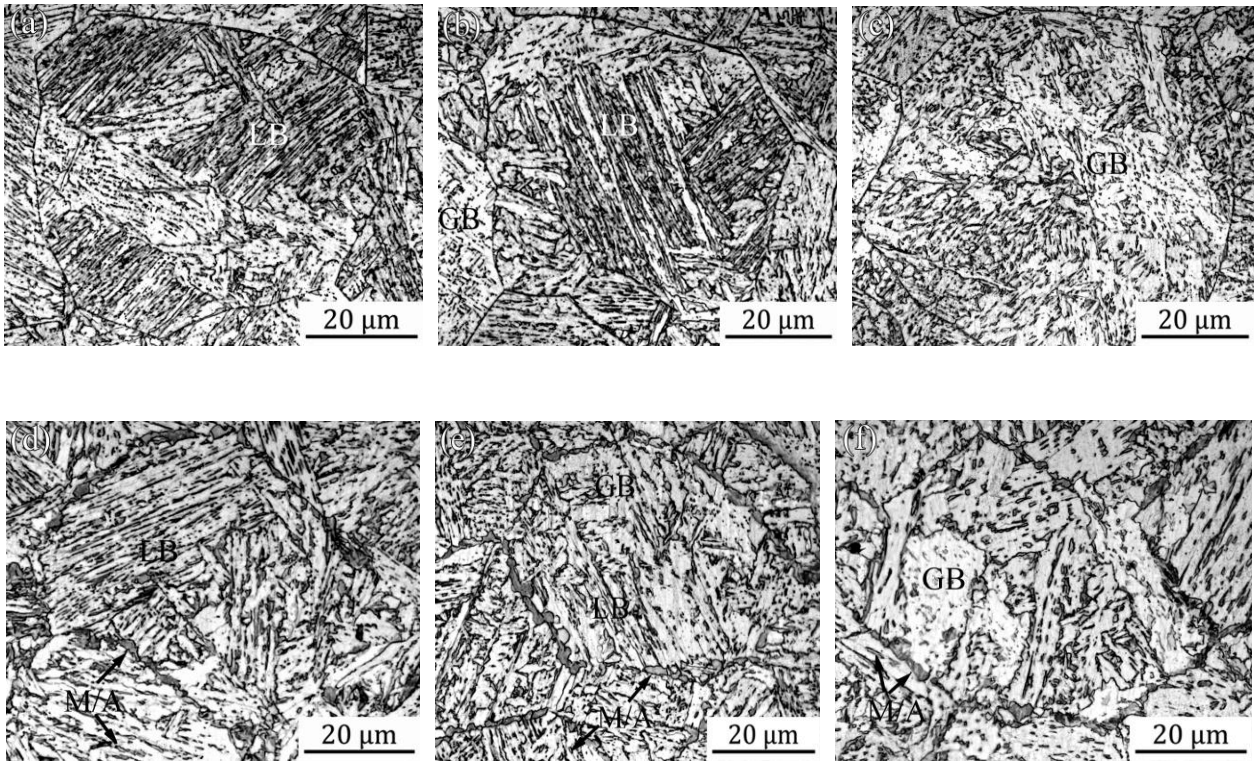

Figure 5. Optical micrographs depicting the microstructure of simulated CGHAZ (a–c) and ICCGHAZ (d–f) with different cooling times: (a,d) $\Delta t_{8/5}$ = 8 s, (b,e) $\Delta t_{8/5}$ = 20 s and (c,f) $\Delta t_{8/5}$ = 50 s.

3.2.2. M/A and crystallographic structure in CGHAZ

Since M/A constituents in CGHAZ can not be plenarily characterized by OM, high-magnification SEM images are shot and shown in Figure 6. With the descend of cooling rate, two apparent differences can be found. One is the change in morphology of M/A constituent, and the other is the variation of average size. Although the average size displays an ascending trend, the values of all the three samples are smaller than 0.8 μm apart from the largest particles (~1.1 μm) displayed in Figure 7. Moreover, the volume fractions of M/A are only ~5.6 ($\Delta t_{8/5}$ = 8 s), 7.2 ($\Delta t_{8/5}$ = 20 s) and 7.7% ($\Delta t_{8/5}$ = 50 s), respectively. That is to say that the shaping of the morphology should be more worthy of attention. From Figure 6a to c, it can be confirmed that the morphology of M/A constituent changes from film-shape to block-shape. Additionally, this variation can also be described from the aspect of ratio on long/short axis of M/A, as shown in Figure 7.

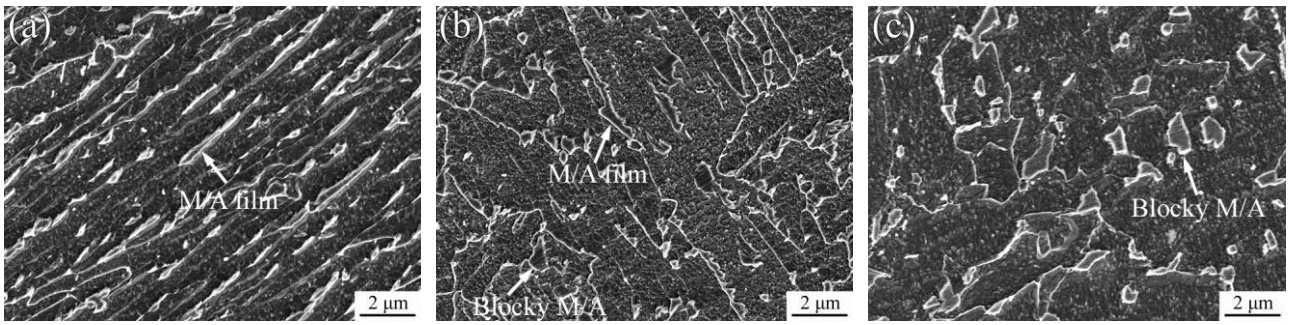

Figure 6. SEM images showing the M/A evolution in CGHZA with different cooling times: (a) $\Delta t_{8/5}$ = 8 s, (b) $\Delta t_{8/5}$ = 20 s and (c) $\Delta t_{8/5}$ = 50 s.

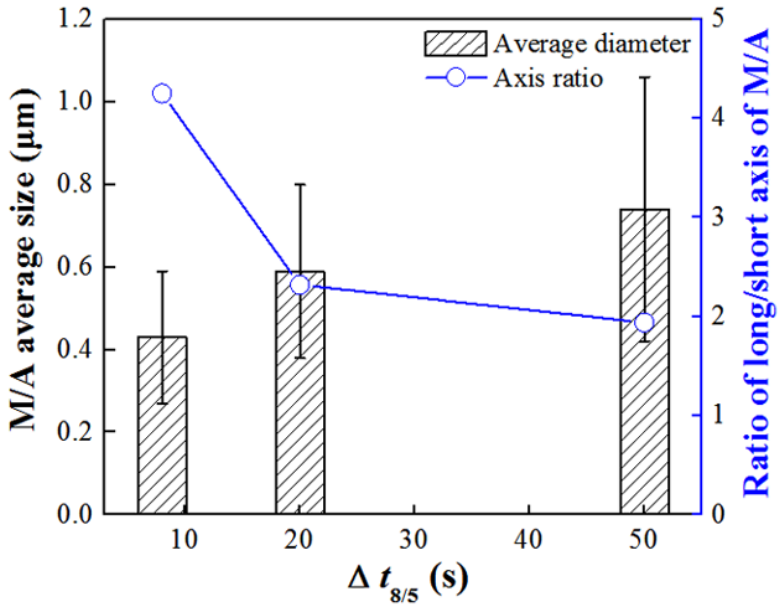

Figure 7. M/A size and morphology of CGHAZ displayed by the ratio of long/short axis.

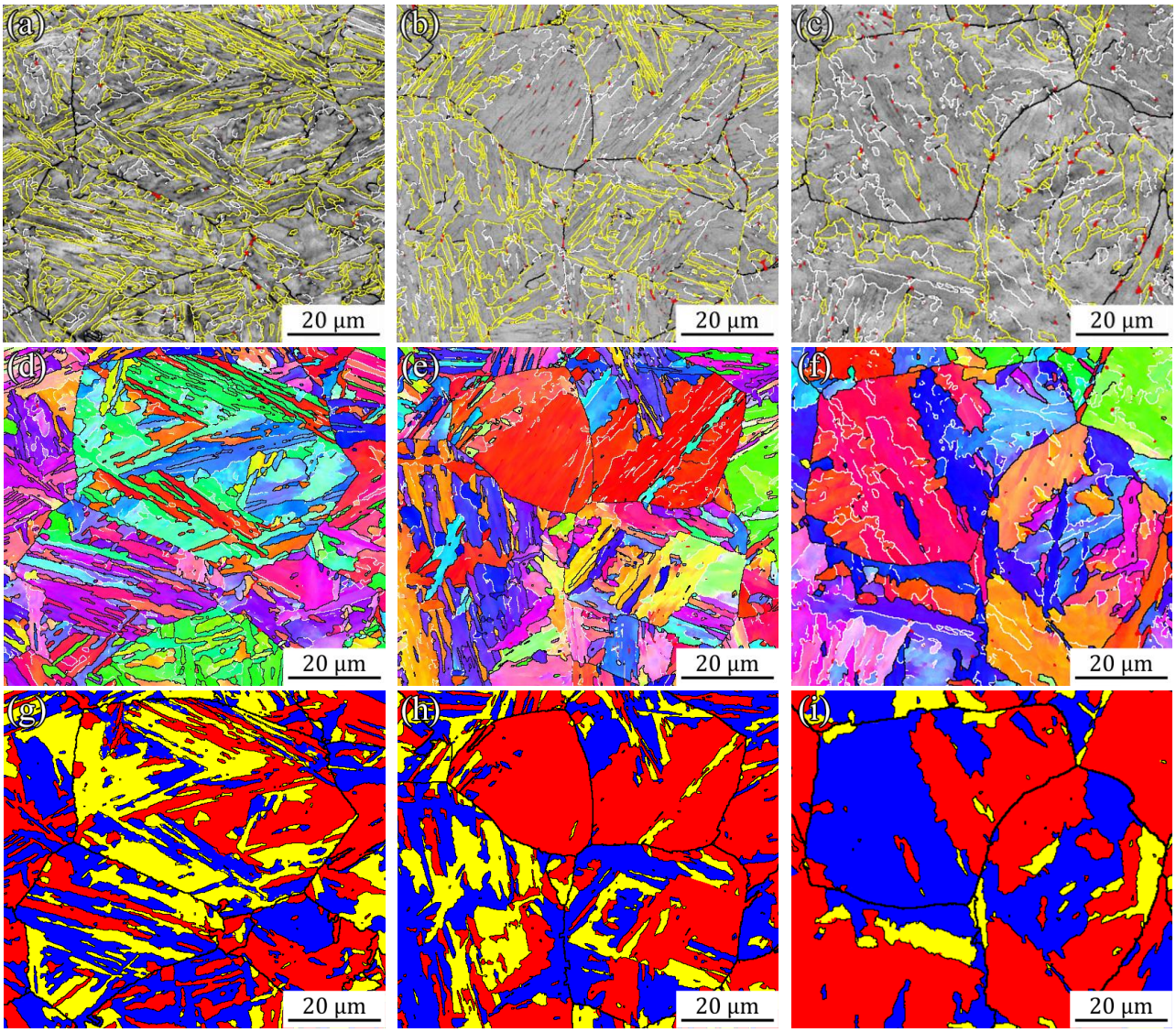

Figure 8. EBSD images showing the distribution of high angle grain boundaries (a–c), and the morphology of crystallographic structures from aspect of inverse pole figure (IPF) (d–f) and Bain zone mapping (d–f) in CGHAZ: (a,d,g) $\Delta t_{8/5}$ = 8 s, (b,e,h) $\Delta t_{8/5}$ = 20 s and (c,f,i) $\Delta t_{8/5}$ = 50 s.

Previous study [17] suggested that M/A with thickness of ~20 nm could deflect brittle cracks and is good for impact toughness. Moreover, the critical size of M/A constituents that could deteriorate the impact toughness should be larger than ~1.3–2 μm [18], meaning that the M/A size in CGHAZ should not be the dominant factor that contribute to the variation of impact toughness. Since the crystallography is the most intrinsic aspect of the microstructure, the impact toughness would be partially affected by the crystallography. Therefore, the other influential factor, i.e. crystallographic structure was analyzed. Just as our previous study [19] and other works [20–22] proposed that the global change of the crack propagation path was mainly attributed to the boundaries of Bain zone, rather than by packet boundary. The Bain maps highlighted with three differential colors corresponding to three Bain groups were shown in Figure 8, together with boundary distribution maps and inverse pole figures (IPF) visualized the crystallographic structures. The boundaries with

differential misorientation angles in boundary distribution maps are dispalyed correspondingly with different colors (misorientation: θ, white lines: 5 °< θ <15 °, black lines: 15 °< θ < 45 °, yellow lines: θ > 45 °), while for Bain maps the boundaries of Bain zone and prior austenite grain are respectively shown by black lines with misorientation angles larger than 45 °. In inverse pole figures, the boundaries of crystallographic structures are displayed by low (white lines: 5 °< θ < 15 °) and high (black lines: θ > 15 °) misorientation. The results suggested in the Boundary-Frequency distribution maps (Figures 8a–c and Figure 9a) indicated that the frequency of high angle grain boundaries (θ > 45 °) decreases dramatically with the descending of cooling rate. Moreover, the morphology of Bain zones change from interleaved needle-like type to consolidated massive type, implying the variant selection policies varied. In the samples cooled with high rate, the driving force for bainite transformation are great as well. Since the cooling rate lowered, the driving force dropped simultaneously and subsequently promoted more variants from the same Bain group. Consequently, one or two predominant Bain zones are formed in a single austenite grain (red and blue Bain zones in Figure 8i) [23]. It means that the effective grain size becomes coarser, which can also be concluded from the size distribution and average diameters of Bain zones shown in Figure 9b. Figure 9c gives the actural density of high angle grain boundaries (defined with boundary length per unit area), which is consistent with the results of the size of Bain zones. The coarser the Bain zones, the lower the density of high angle grain boundaries. As the boundaries with misorientation between 15 ° and 45 ° are primarily prior austenite grain boundaries, there is no significant variation in these three values and the values are also small. Moreover, the decrement in density of low angle grain boundaries (θ < 15 °) is due to the coarsen of bainitic lath, corresponding to the results of SEM. While, another interesting thing is the augment of the volume fraction of fcc phase i.e, reatined austenite (red dots in boundary distribution maps) with decreasing in cooling rate, which is similar to the change in M/A constituents. Previous study [24] showed that retained austenite as one part of M/A constituents can be obtained in room temperature, and the increasing tendency suggests the transformation that took place in higher cooling rate is much more complete than that in low cooling rate.

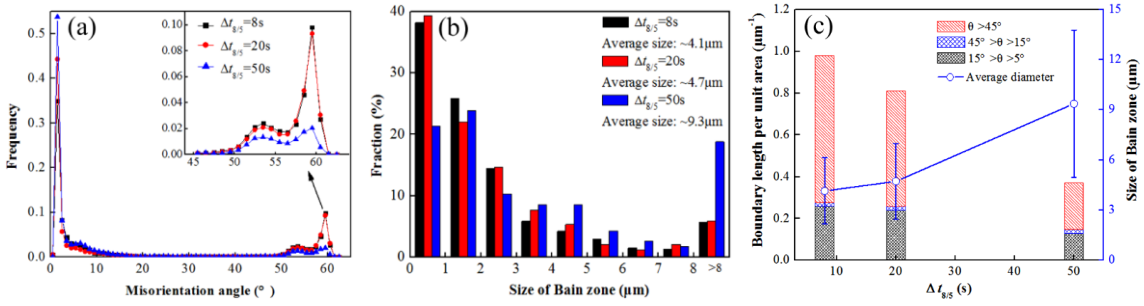

Figure 9. Grain boundaries distribution showed by frequency (a) and density ((c), boundary length per unit area), and size distribution of crystallographic Bain zones (b) corresponding to Figure 7d–f.

3.2.3. M/A and high angle grain boundary in ICCGHAZ

EBSD characterizations of ICCGHAZ with high and low cooling rates are shown in Figure 10. The evolution in density of grain boundaries is agreed with the results in CGHAZ. The similarities to the CGHAZ lie in two aspects. Firstly, in the samples cooled with high rates, high density of highly misoriented grain boundaries are formed. Secondly, the shaping of the crystallographic structure and the configuration manner of the differential Bain groups in both cases are analogous as well, implying the effect of precursor microstructural heredity is fascinating. The major difference emerged in ICCGHAZ and CGHAZ is the large amounts of necklace-shape M/A constituents formed along the prior austenite grain boundaries. The average size of necklace-shape M/A constituents can be up to 2 μm, which is much coarser than the dispersed M/A within the prior austenite grain. Moreover, the stress concentration in coarse M/A constituents is higher than that in bainite, meaning that a local brittle zone (LBZ) will be formed in ICCGHAZ, which in turn will bring about local unstable fracture [25,26] and seriously deteriorate the low temperature toughness of the entire weld joint. It should be noticed that there is no visible change in the size of necklace-type M/A or dispersed M/A with lower cooling rate. That means the variation of high angle grain boundaries should be account for the slight decline of impact toughness in ICCGHAZ, while the dramatic decline in toughness from CGHAZ to ICCGHAZ was due to the formation of necklace-type M/A constituents.

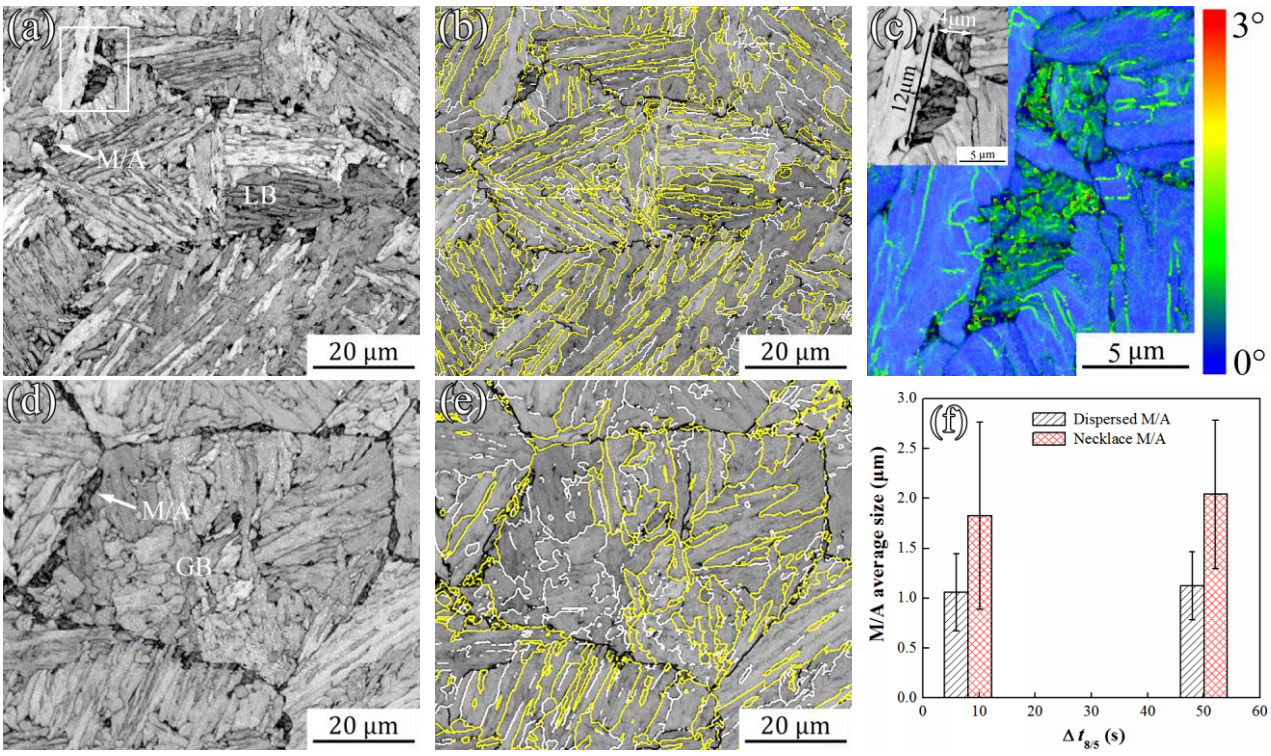

Figure 10. EBSD images showing the distribution of high angle grain boundaries (a–c) and the morphology of crystallographic packet (d–f) and block (g–i) in CGHAZ. (a,d,g) $\Delta t_{8/5}$ = 8 s, (b,e,h) $\Delta t_{8/5}$ = 20 s and (c,f,i) $\Delta t_{8/5}$ = 50 s.

3.3. Correlation of crystallographic structure and crack propagation

It is well know that the impact toughness associated much to the abilities of crack initiation and propagation, which are primarily correlated to the brittle phase (M/A constituents) and crystallographic structure (high angle grain boundaries) in ICCGHAZ and CGHAZ. Therefore, the further investigations will focus on the crack initiation and propagation in the viewpoint of crystallography, considering the fact that the phase of microstructure is intrinsically crystal. EBSD images for the secondary cracks obtained from the fractured V-notch Charpy samples of CGHAZ and ICCGHAZ with high and low cooling rates are displayed in Figures 11 and 12. From Figure 11 it can be found that in different crystallographic structures induced by cooling rates, adverse crack propagation paths occurred. This diversity embodied in the size and morphology of the cracks (Figure 11a and d). Under high cooling condition, fine uniformly intersecting configured Bain zones that would form high angle grain boundaries were formed. They effectively deflected or arrested the brittle crack propagation and thus yielded multi-inflection cracks with short length, indicating more energies would be absorbed during crack propagation. In contrast, coarse Bain zones (yellow Bain zone in Figure 11f) that could easily provide a favorable path for crack propagation were formed at low cooling rate, and the crack would propagate throughout the entire Bain zone. It can be stopped only at the boundaries of Bain zone or prior austenite grain, resulting in a straight crack with large size and low absorbed energy. However, despite the size of Bain zones are quite differential, the configuration manner of the Bain zones are identical. Another finding is worth noting that the resistance of crack propagation or deflection angle seems to be related to the thickness of Bain zone, promoting a small angle to the direction of crack propagation. When the thickness is lower than a certain value, the resistance or deflection angle gets small, as shown by arrows in Figure 11c. Although another study [27] certified that the crack path in ferritic steel is related to the crystallographic misorientation between the neighboring grains when brittle cracks go through boundaries, and high angle grain boundaries in some particular cases could scarcely deflect or arrest the crack propagation, it has not been validated in bainitic steel. Moreover, the local change in crack path can also occur at these Bain zone boundaries, but nonlinear penetration. Therefore, we can conclude that the size of Bain zone could control the absorbed energy in process of cleavage fracture, though the size or misorientation effect is not very clear.

For ICCGHAZ (Figure 12), the patterns of crack propagation in samples with high or low cooling rates are the same as CGHAZ. Global or local changes in crack path simply occurred at the boundaries of Bain zone or prior austenite grain. While, the crack initiation at prior austenite grain boundary necklaced by coarse M/A constituents was observed in ICCGHAZ, as shown in Figure 12d. In the viewpoint of crack initiation from necklace-type M/A, four possible mechanisms are collated by Davis [5], which are (i) M/A particle is a brittle phase and cracks readily; (ii) transformation to M/A induces residual tensile stress in the surrounding ferrite matrix which assists cleavage; (iii) M/A with higher hardness than the surrounding ferrite will induce stress concentration in the neighboring ferrite matrix during external deformation, and thereby assists cleavage fracture; (iv) micro-cracks forming on the debonded M/A and matrix interface propagate via the linking of other debonded regions. In this study, the crack initiated at necklace-type M/A constituents and then two micro-cracks branching from it were formed, indicating the fracture process should be obeyed the mechanism (iii). This can also be verified by comparison the stress distribution in M/A particles (Figure 10c) and fracture morphology (Figure 4f). Moreover, comparing with the crack propagation

and fracture surface, it can be believed that the obvious varieties in facets of the cleavage fracture region obtained at different cooling rates are attributed to the difference in crystallographic structure, i.e., the size of Bain zone.

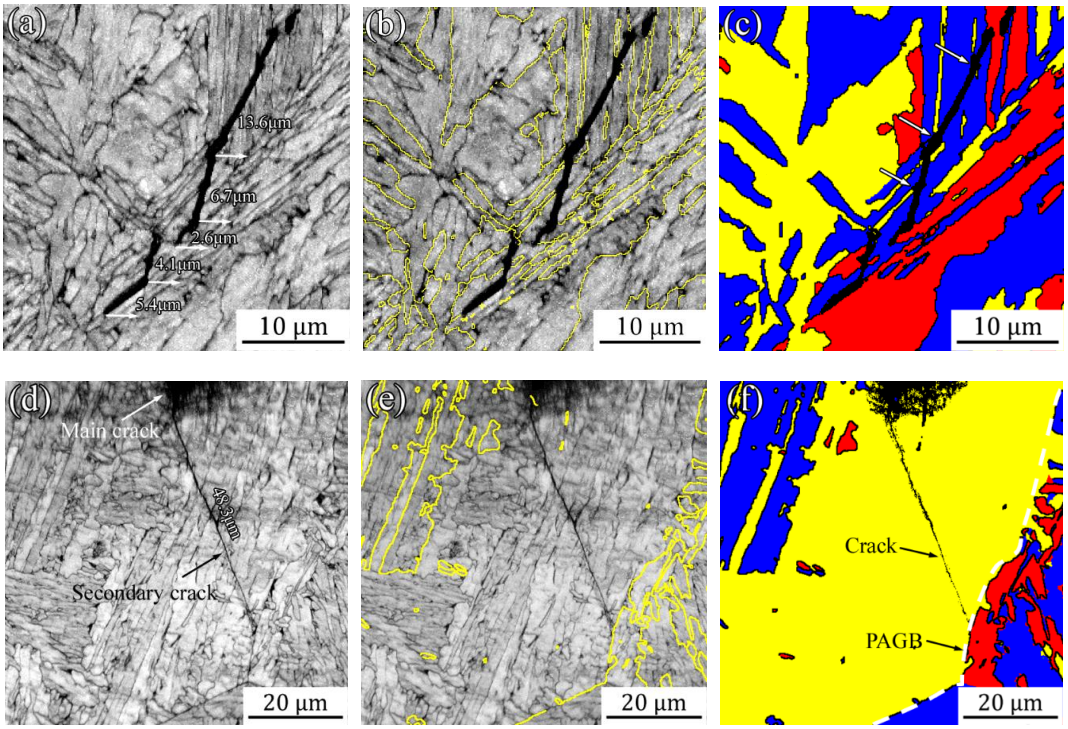

Figure 11. EBSD images (band contrast (BC), boundary distribution (yellow line: θ > 45 °), Bain maps) for the secondary cracks observed on the fractured V-notch Charpy sample of CGHAZ. (a–c) $\Delta t_{8/5}$ = 8 s and (d–f) $\Delta t_{8/5}$ = 50 s.

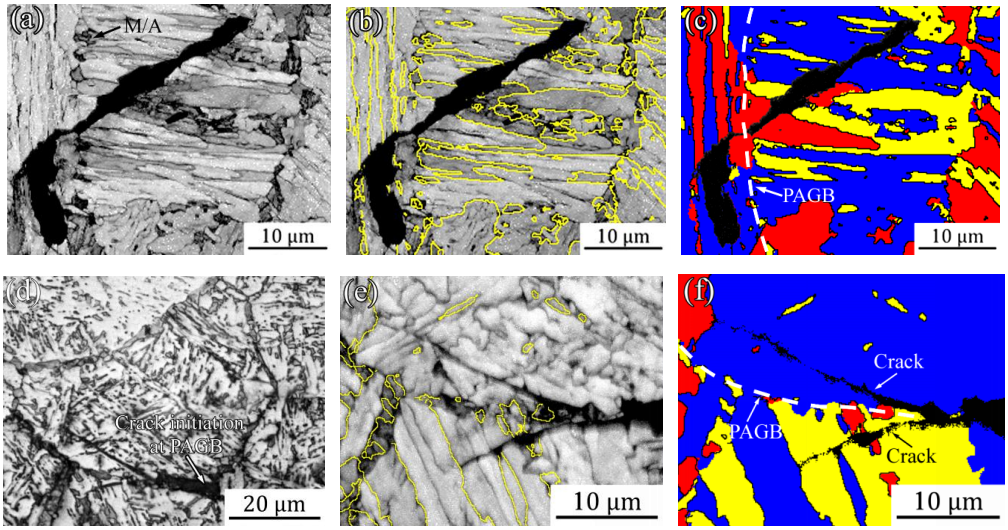

Figure 12. OM and EBSD images (band contrast (BC), boundary distribution (yellow line: θ > 45 °), Bain maps) for the secondary cracks observed on the fractured V-notch Charpy sample of ICCGHAZ. (a–c) $\Delta t_{8/5}$ = 8 s and (d–f) $\Delta t_{8/5}$ = 50 s.

3.4. Over-all discussion on correlation between microstructure and impact toughness

The above analysis on microstructural evolution and crack propagation in CGHAZ and ICCGHAZ suggested that the final impact energy of CGHAZ is primarily determined by the size of Bain zone enclosed by high angle grain boundaries and the M/A constituents, which is significantly influenced by cooling rate. The increase in hardenability caused by increased cooling rate promotes more crystallographic variants from different Bain groups. Meanwhile, combination with controlling inter-spacing of Bain zone boundaries by self-accommodation below the critical Griffith crack length, micro-crack can be arrested by these high angle grain boundaries and thereby suppressed the brittle fracture initiation and increased the ductile regions [28]. However, for ICCGHAZ, the impact energy is dominantly governed by M/A constituents, especially coarse necklace-type M/A constituents, and the influence caused by cooling rate is slight. That means the impact toughness of CGHAZ could be controlled more easily than the ICCGHAZ in terms of actual engineering, considering that the transformation of CGHAZ is more sensitive to the heat input than the ICCGHAZ during welding [9–11]. Since the ICCGHAZ was formed in the second welding thermal cycle and was unavoidable for dual-pass welding, it made it almost impossible for the ICCGHAZ to regulate the microstructure and toughness by changing welding parameters. The critical point is how to inhibit the formation of necklace-type M/A constituents or how to control the size and fraction once they were transformed. Previous studies [29] suggested that these necklace-type M/A constituents can also be formed in reheated zone of multi-pass weld metal. But fortunately, four feasible methods are also proposed in recent studies, which are (i) via increase of Ni in the matrix to promote the transformation of austenite more completely during welding and thus reduce the appearance of M/A constituents [24]; (ii) through refinement of prior austenite grain size in CGHAZ to control the size of necklace-type M/A products formed in ICCGHAZ [16]; (iii) by self-tempering in multi-pass welding process to decompose the formed necklace-type M/A constituents [29]; (iv) through post-weld heat treatment, especially inter-critical heat treatment to promote the reversion of M/A constituents and formation of certain content of retained austenite by twice enrichment of Mn and Ni [30]. Although there exists some limitations in applying the above four methods such as cost growth, aggressive control of welding process and application fields, it is indisputable that they can effectively control the formation and distribution of necklace-type M/A constituents and enhance the impact toughness.

Another technical route to control the properties from base plate to heat affected zone including CGHAZ and ICCGHAZ is using of niobium, despite that it has not yet been plenarily proved. The complex high-temperature (Ti, Nb)N-Nb(C, N) and strain-induced NbC precipitates were firstly obtained in hot rolled plate by precipitation. During welding, the fine NbC will be fleetly dissolved into the matrix, while coarse (Ti, Nb)N-Nb(C, N) particles with a given inter-spacing would be retained and thus exerts a larger Zener pinning pressure to prevent austenite grain coarsening, thereby resulting in a finer limited austenite grain size in CGHAZ [31,32]. Moreover, the soluted Nb can retard the austenite to ferrite transformation and facilitate bainite transformation to obtain an optimum crystallographic structure [33,34]. In the second welding thermal cycle, the finer austenite grain obtained in CGHAZ is beneficial to suppress the formation of coarse necklace-type M/A and consequently give a good toughness in ICCGHAZ [18].

4. Conclusions

The level of the cooling rate effect on impact toughness in ICCGHAZ and CGHAZ is dramatic. Evident enhancement of toughness in CGHAZ can be achieved by increasing the cooling rate, whereas it is scarcely accessible for ICCGHAZ. It was due to that the kernel factor controlling the toughness of CGHAZ was crystallographic structures at differential cooling rates, while it transited to the necklace-type M/A constituents formed in the second thermal cycle and unconcerned to the precursor microstructure.

The slight increase in impact toughness in ICCGHAZ with increasing cooling rate is primarily attributed to the heredity of precursor microstructure. While, the reduction in impact toughness from CGHAZ to ICCGHAZ is due to the formation of necklace-type M/A constituents along the prior austenite grain boundaries.

The analyses on crystallographic feature and secondary crack propagation indicated that Bain zone should be confirmed as the effective grain from the crystallography, which can effectively deflect or arrest the brittle crack propagation. Coarse Bain zone will promote large and straight crack, resulting in large fracture facet and low absorbed energy. Moreover, the resistance of crack propagation yielded by over-fine Bain zone is slight because of the small angle of deflection in the direction of crack propagation.

Acknowledgement

The authors acknowledge the support from National Key Research and Development Project of China (2017YFB0304900), the China Scholarship Council (CSC) for the award of a scholarship to Xuelin Wang for studies at McMaster University, thanks to Glynis de Silveira and Chris Butcher in Canadian Centre for Electron Microscopy (CCEM) for the technical support with electron microscopy, and thanks to Cyril Cayron for the support of ARPGE software.

Conflict of interest

The authors declare that there is no conflict of interests regarding the publication of this paper.

References

1. D. S. Liu, Q. L. Li and T. Emi, Microstructure and mechanical properties in hot-rolled extra high-yield-strength steel plates for offshore structure and shipbuilding, *Metall. Mater. Trans. A*, **42** (2011), 1349–1361.
2. Y. L. Zhou, T. Jia, X. J. Zhang, et al., Microstructure and toughness of the CGHAZ of an offshore platform steel, *J. Mater. Process. Tech.*, **219** (2015), 314–320.
3. Y. You, C. J. Shang, L. Chen, et al., Investigation on the crystallography of the transformation products of reverted austenite in intercritically reheated coarse grained heat affected zone, Mater. Des., **43** (2013), 485–491.
4. X. D. Li, X. P. Ma, S. V. Subramanian, et al., Structure-property-fracture mechanism correlation in heat-affected zone of X100 ferrite-bainite pipeline steel, *Metall. Mater. Trans. E*, **2** (2015), 1–11.

5. C. L. Davis and J. E. King, Cleavage initiation in the intercritically reheated coarse grained heat affected zone, *Metall. Mater. Trans. A*, **25** (1994), 563–573.
6. A. Lambert-Perlade, A. F. Gourgues, J. Besson, et al., Mechanisms and modeling of cleavage fracture in simulated heat-affected zone microstructures of a high-strength low alloy steel, *Metall. Mater. Trans. A*, **35** (2004), 1039–1053.
7. Y. Li and T. N. Baker, Effct of morphology of martensite-austenite phase on fracture of weld heat affected zone in vanadium and niobium microalloyed steels, *Mater. Sci. Technol.*, **26** (2010), 1029–1040.
8. L. Y. Lan, C. L. Qiu, D. W. Zhao, et al., Microstructural characteristics and toughness of the simulated coarse grained heat affcted zone of high strength low carbon bainitic steel, *Mater. Sci. Eng. A*, **529** (2011), 192–200.
9. Y. You, C. J. Shang, W. J. Nie, et al., Investigation on the microstructure and toughness of coarse grained heat affected zone in X-100 multi-phase pipeline steel with high Nb content, *Mater. Sci. Eng. A*, **558** (2012), 692–701.
10. Z. X. Zhu, J. Han and H. J. Li, Influence of heat input on microstructure and toughness properties in simulated CGHAZ of X80 steel manufactured using high-temperature processing, *Metall. Mater. Trans. A*, **46** (2015), 5467–5475.
11. J. Hu, L. X. Du, J. J. Wang, et al., Effect of welding heat input on microstructures and toughness in simulated CGHAZ of V-N high strength steel, *Mater. Sci. Eng. A*, **577** (2013), 161–168.
12. X. D. Li, Y. R. Fan, X. P. Ma, et al., Influence of martensite-austenite constituents formed at different intercritical temperatures on toughness, *Mater. Des.*, **67** (2015), 457–463.
13. X. D. Li, X. P. Ma, S. V. Subramanian, et al., EBSD characterization of secondary microcracks in the heat affected zone of a X100 pipeline steel weld joint, *Int. J. Fract.*, **193** (2015), 131–139.
14. X. D. Li, C. J. Shang, X. P. Ma, et al., Elemental distribution in the martensite-austenite constituent in intercritically reheated coarse-grained heat-affected zone of a high-strength pipeline steel, *Script. Mater.*, **139** (2017), 67–70.
15. X. D. Li, C. J. Shang, X. P. Ma, et al., Structure and crystallography of martensite-austenite constituent in the intercritically reheated coarse-grained heat affected zone of a high strength pipeline steel, *Mater. Charact.* **138** (2018), 107–112.
16. C. Cayron, ARPGE: a computer program to automatically reconstruct the parent grains from electron backscatter diffraction data, *J. Appl. Cryst.*, 40 (2007), 1183–1188.
17. Y. Zhong, F. R. Xiao, J. W. Zhang, et al., In situ TEM study of the effect of M/A films at grain boundaries on crack propagation in an ultra-fine acicular ferrite pipeline steel, *Acta Mater.*, **54** (2006), 435–443.
18. X. D. Li, X. P. Ma, S. V. Subramanian, et al., Influence of prior austenite grain size on martensite-austenite constituent and toughness in the heat affected zone of 700 MPa high strength linepipe steel, *Mater. Sci. Eng. A*, **616** (2014), 141–147.
19. X. L. Wang, Z. Q. Wang, X. P. Ma, et al., Analysis of impact toughness scatter in simulated coarse-grained HAZ of E550 grade offshore engineering steel from the aspect of crystallographic structure, *Mater. Charact.*, **140** (2018), 312–319.
20. H. Terasaki, Y. Shintome, Y. I. Komizo, et al., Effect of close-packed plane boundaries in a Bain zone on the crack path in simulated coarse-grained HAZ of bainitic Steel, *Metall. Mater. Trans. A*, **46** (2015), 2035–2039.

21. H. Terasaki, Y. Miyahara, M. Ohata, et al., Visualization of microstructural factor resisting the cleavage-crack propagation in the simulated heat affected zone of bainitic Steel, *Metall. Mater. Trans. A*, **46** (2015), 5489–5493.
22. M. Tsuboi, A. Shibata, D. Terada, et al., Role of different kinds of boundaries against cleavage crack propagation in low-temperature embrittlement of low-carbon martensitic steel, *Metall. Mater. Trans. A*, **48** (2017), 3261–3268.
23. X. L. Wang, Z. Q. Wang, L. L. Dong, et al., New insights into the mechanism of cooling rate on the impact toughness of coarse grained heat affected zone from the aspect of variant selection, *Mater. Sci. Eng. A*, **704** (2017), 448–458.
24. Y. You, C. J. Shang and S. Subramanian, Effect of Ni addition on toughness and microstructure evolution in coarse grain heat affected zone, *Met. Mater. Int.*, **20** (2014), 659–668.
25. F. Matsuda, K. Ikeuchi, Y. Fukada, et al., Review of Mechanical and Metallurgical Investigations of M-A Constituent in Welded Joint in Japan, *Trans. JWRI.*, **24** (1995), 1–24.
26. R. Danilo and G. Vladimir, Simulations of transformation kinetics in a multi-pass weld, *Mater. Manuf. Process.*, **20** (2005), 833–849.
27. A. Ghosh, S. Kundu and D. Chakrabarti, Effect of crystallographic texture on the cleavage fracture mechanism and effective grain size of ferritic steel, *Scr. Mater.*, **81** (2014), 8–11.
28. S. V. Subramanian, X. P. Ma and L. Collins, Structure-property studies on HAZ toughness of niobium microalloyed linepipe steels, 6th International Pipeline Technology Conference, Ostend, October, (2013), 1–25.
29. X. L. Wang, Y. R. Nan, Z. J. Xie, et al., Influence of welding pass on microstructure and toughness in the reheated zone of multi-pass weld metal of 550 MPa offshore engineering steel, *Mater. Sci. Eng. A*, **702** (2017), 196–205.
30. X. L. Wang, X. M. Wang, C. J. Shang, et al., Characterization of the multi-pass weld metal and the impact of retained austenite obtained through intercritical heat treatment on low temperature toughness, *Mater. Sci. Eng. A*, **649** (2016), 282–292.
31. X. P. Ma, X. D. Li, B. Langelier, et al., Effects of carbon variation on microstructure evolution in weld heat-affected zone of Nb-Ti microalloyed steels, *Metall. Mater. Trans. A*, **49** (2018), 4824-4837.
32. A. D. Schino and P. E. D. Nunzio, Effect of Nb microalloying on the heat affected zone microstructure of girth welded joints, *Mater. Lett.*, **186** (2017), 86–89.
33. C. Fossaert, G. Rees, T. Maurickx, et al., The effect of niobium on the hardenability of microalloyed austenite, *Metall. Mater. Trans. A*, **26** (1995), 21–30.
34. G. I. Rees, J. Perdrix, T. Maurickx, et al., The effect of niobium in solid solution on the transformation kinetics of bainite, *Mater. Sci. Eng. A*, **194** (1995), 179–186.

AIMS Press